

Research Article

Surface roughness, material removal rate, and their multi-objective optimization in the dry turning of Mg-4Zn/Si₃N₄ nanocomposites by PCD tool

N Anand^{1,2,*}, K Jayaprakash Reddy³, D Bijulal^{2,4}, K Vijayan³, P Prasanth³

¹Department of Mechanical Engineering, College of Engineering Trivandrum, Engineering College P.O, Sreekaryam, Thiruvananthapuram, Kerala, 695016, India

²APJ Abdul Kalam Technological University, Thiruvananthapuram, CET Campus, Thiruvananthapuram Kerala, 695016, India

³ISRO Inertial Systems Unit, Vattiyoorkavu PO, Thiruvananthapuram, Kerala, 695013, India

⁴Department of Mechanical Engineering, Government Engineering College Barton Hill, Kunnukuzhi, Thiruvananthapuram, Kerala, 695035, India

*e-mail: anandlight.win@gmail.com

Submitted: 19/05/2025 Revised: 07/07/2025 Accepted: 15/07/2025 Published online: 28/07/2025

Abstract: To manufacture useful products with good surface quality from the sustainable Mg-4Zn/Si₃N₄ nanocomposites strengthened by Si₃N₄ nanoparticles, machining after stir casting is needed, and it has to be done economically. The Si₃N₄ nanoparticles could influence the machining behavior due to their abrasive properties and their ability to strengthen the alloy matrix. Multi-objective optimization of material removal rate (*MRR*) (a good indicator of economic production) and surface roughness (*R_a*) (a good indicator of quality of surface) are necessary to identify the optimal settings. This research reports the dry turning studies of vacuum stir cast Mg-4Zn/Si₃N₄ nanocomposites with a polycrystalline diamond turning tool. Response surface methodology (RSM)-based Box-Behnken design was used. The reinforcement (nanometre-sized silicon nitride) weight percentage, cutting speed, feed rate, and depth of cut were the input factors. Regression models for prediction of material removal rate (*MRR*) and surface roughness (*R_a*) were obtained and validated. Multi-objective optimization of *MRR* and *R_a* using Design-Expert software identified a reinforcement of 0.44 wt.% and a cutting speed of 110 m/min, a feed rate of 0.09 mm/rev, and a depth of cut of 0.16 mm as the optimal settings. The effects of the input process parameters on the *MRR* and *R_a* are also studied.

Keywords: Mg-4Zn; Si₃N₄; Nanocomposite; Machining; Optimization

I. INTRODUCTION

The development and production of magnesium (Mg)-based products have become extremely important in various areas of application in the present era. In the automobile and aerospace sectors, they are preferred because of low density (1.74 g/cm³), higher specific stiffness, and specific strength. The use of such lightweight materials and products enhances sustainability [1] and helps to minimize the emission of greenhouse gases and is also cost-effective [2]. Mg-based materials are also promising candidates for hydrogen storage applications due to their abundance, low cost, and good capacity to store hydrogen [3]. Their

uniqueness comes in combining these properties with good biocompatibility, biodegradability, and bioresorbability [4], which makes them good candidates as biomedical materials too. They are also preferred for some electronic applications [3]. In spite of the various advantages, further improvements of their properties are mostly necessary to enhance their application potential. This is possible by the use of ceramics as reinforcements in Mg-based matrices to form metal matrix composites (MMCs) [5], which possess improved strength, wear resistance, dimensional stability, and also properties at high temperatures [6]. It is therefore important to produce functional

components from MMCs for use in many applications.

Stir casting is a simple and flexible method to produce components from the MMCs [7]. However, to achieve dimensional accuracy and surface finish specifications, these components need subsequent machining. But since the reinforcements have an abrasive nature, and they also increase the hardness of the MMCs [8], turning MMC becomes challenging. It is important to study the effects of the reinforcements in the turning of Mg-based MMCs. Moreover, optimizing the machining parameters is critical to save energy and ensure sustainability [9] in the manufacturing of Mg MMCs. Crucial indicators of the machining process and product quality are chosen as the responses for optimization. Surface roughness is one such indicator of product quality that influences the frictional and tribological characteristics of the product and also influences its life and efficiency. A high material removal rate (another crucial indicator of machining) is necessary for economically viable large-scale production [10]. Various aspects of machining Mg-based materials have been investigated by researchers. Abbas et al. [11] investigated the turning of AZ61 Mg alloy with depth of cut, cutting speed, and feed rate as input factors and optimized the surface roughness. Kumar et al. [12] utilized *MRR* and surface roughness to optimize the thermoelectric machining of Mg composite reinforced with Al and SiC. Sudhagar et al. [13] performed multi-objective optimization of surface roughness and kerf width in the wire electric discharge machining of magnesium composite reinforced with BN and Si_3N_4 .

Among the various Mg-based materials, the Mg alloy with 4 wt.% Zn (Mg-4Zn) possesses a good combination of low degradation rate, biocompatibility, and moderate mechanical properties, [14], [15], [16]. It has research scope for property improvement by the addition of Si_3N_4 ceramic particles. Silicon nitride (Si_3N_4) possesses good wear resistance, thermal stability, and mechanical properties and is used in rollers, rotors, and ball bearings [17] and has been used to improve properties of various materials [18].

This research hypothesizes that the addition of Si_3N_4 nanoparticles to improve the properties of Mg-4Zn alloy will also influence its machining behavior. **Fig. 1** shows the highlights of this research. This research deals with manufacturing of sustainable lightweight Mg-4Zn nanocomposites reinforced with small fractions of nano- Si_3N_4 (a biocompatible bioceramic [19]). Machining experiments are conducted based on response surface methodology-based Box-Behnken design with a polycrystalline diamond (PCD) turning tool, which produces high-quality surfaces in the machining of difficult-to-machine materials, has low friction properties, and has high hardness [20]. Regression models are

developed and validated for *MRR* and R_a . Multi-objective optimization of *MRR* and R_a is performed to arrive at the optimal setting.

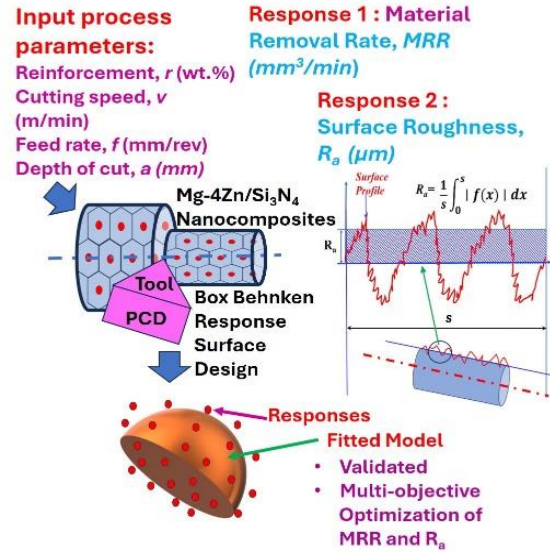


Figure 1. Highlights of this research

II. MATERIALS AND METHODS

Vacuum stir cast Mg-4Zn/ Si_3N_4 nanocomposites (**Fig. 2**) are used for the machining studies. A bottom-pouring stir casting machine (SwamEquip make) under argon gas protection was used for the vacuum stir casting. Mg and Zn ingots were melted in the desired proportion in the furnace at 750 °C.

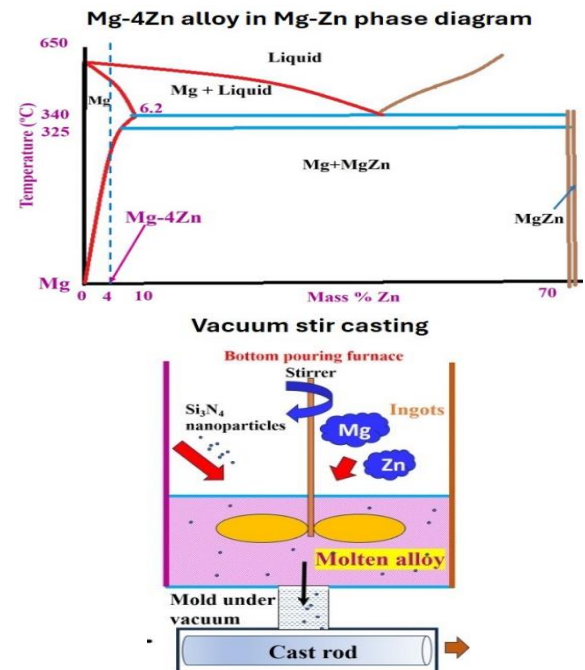


Figure 2. Vacuum stir casting of Mg-4Zn/ Si_3N_4 nanocomposites

Nanoshel-made Si_3N_4 nanoparticles (reinforcement) of 15-30 nm average particle size were then added to the melt in the desired proportion by

wrapping in Al foil. The melt was stirred at 500 rpm for 10 minutes for uniformly distributing the constituents. The melt was poured into a preheated steel mold under vacuum and removed after solidification. This procedure was followed with 0.23, 0.45, and 0.67 wt.% Si_3N_4 reinforcements to produce Mg-4Zn nanocomposites. Specimens extracted from the castings after surface preparation were observed under an optical microscope (Dewinter-made) and a ZEISS-made scanning electron microscope (SEM). **Fig. 3** shows the SEM elemental maps and optical micrographs of the nanocomposites.

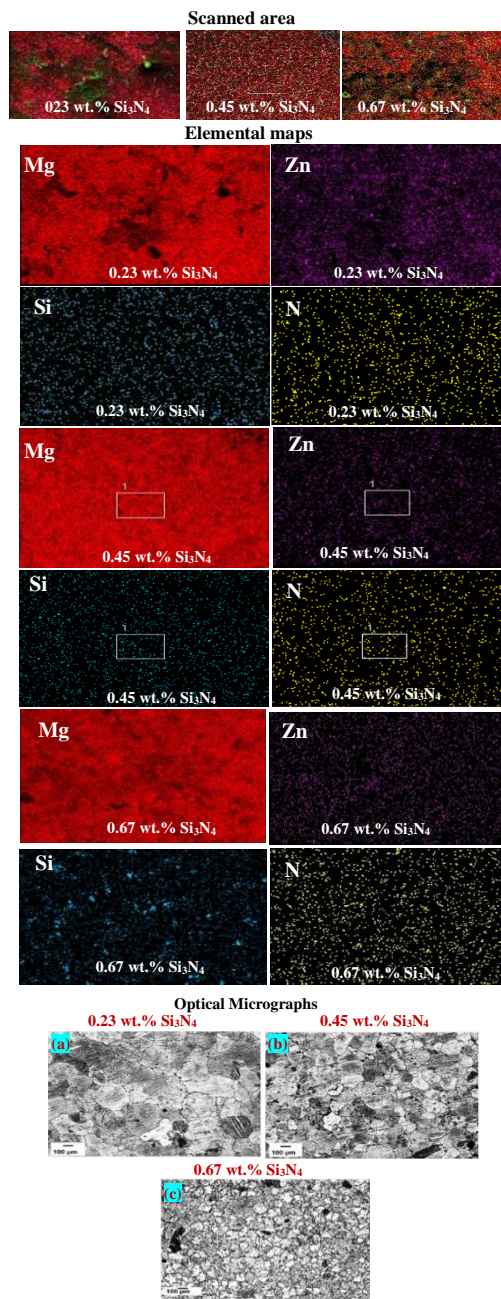


Figure 3. SEM elemental maps of Mg, Z, Si, and N, optical micrographs of the nanocomposites

The surface preparation was done by polishing with emery sheets and then with alumina powder and then etching with acetic picral obtained by mixing 10 ml acetic acid, 10 ml water, 70 ml ethanol, and 4.2 g picric acid. The optical micrographs were utilized to measure the average grain size of 50 grains of each nanocomposite using ImageJ software. Unetched surfaces of the specimens were polished with diamond paste (0.5-1 microns) and subjected to wavelength dispersive X-ray fluorescence spectroscopic (XRF) studies in a Bruker S8 Tiger Series II 4kW machine. Microhardness of these specimens (average of five readings) was measured under a load of 500 g applied for 15 seconds in FIE made microhardness tester. The density was obtained from their weight (measured by a Mettler Toledo weighing balance capable of measuring ± 0.0001 g) using equation (1).

$$\rho_{\text{specimen}} = \left(\frac{W_{\text{in air}}}{W_{\text{in air}} - W_{\text{in water}}} \right) \times \rho_{\text{of water}} \quad (1)$$

where ρ indicates the density, and W indicates the weight. Porosity was calculated from the density using equation (2).

$$\text{Porosity (\%)} = \left(1 - \frac{\rho_{\text{Actual}}}{\rho_{\text{Theoretical}}} \right) \times 100 \quad (2)$$

Table 1 shows the Mg and Zn wt.% obtained by XRF analysis, density, and porosity. **Table 2** shows the microhardness and grain size of the nanocomposites.

Table 1. XRF analysis, density and porosity of the nanocomposites

| wt.% Si_3N_4 | XRF analysis (wt.%) | | Density (g/cc) | Porosity (%) |
|------------------------------|---------------------|------|----------------|--------------|
| | Mg | Zn | | |
| 0.23 | 95.8 | 3.56 | 1.753 | 2.18 |
| 0.45 | 94 | 3.86 | 1.737 | 3.26 |
| 0.67 | 94.5 | 3.66 | 1.769 | 1.55 |

The porosity levels in all the nanocomposite castings were indicative of good-quality castings.

Table 2. Microhardness and grain size of the nanocomposites

| wt.% Si_3N_4 | Microhardness ($\text{HV}_{0.5}$) | Grain size (μm) |
|------------------------------|-------------------------------------|------------------------------|
| 0.23 | 52.0 | 185.8 |
| 0.45 | 57.5 | 135.8 |
| 0.67 | 66.7 | 74.5 |

It is observed from the SEM elemental maps (**Fig. 3**) that there is homogeneous distribution of the elements Mg, Zn, Si, and N, which means the alloy and Si_3N_4 reinforcement have been homogeneously distributed in the nanocomposites.

Machining experiments were carried out using a Schaublin 180 CCN R-TM A 2-5 high-precision CNC lathe. The dry machining experiments of the nanocomposites were designed by following the Box-Behnken design, which is an efficient design based on the response surface methodology (RSM).

Table 3 shows the input factors (coded and actual values) along with their levels. The principle of RSM is based on equation (3), where y indicates the response, ϕ_0 is a constant, ϕ_i 's are the coefficients of the linear terms, and ϕ_{ii} 's and ϕ_{ij} 's are the coefficients of the square and interaction terms, respectively. ϵ is the error in observations. RSM fits a second-order model to the response values (**Fig. 1**) based on the minimizing least squares to develop a mathematical model that connects the responses and the input factors, which are provided in **Table 3**.

$$y = \phi_0 + \sum_{i=1}^4 \phi_i X_i + \sum_{i=1}^4 \phi_{ii} X_i^2 + \sum_{i=1}^3 \sum_{j=1}^4 \phi_{ij} X_{ij} + \epsilon \quad (3)$$

Table 3. Input factors and their levels

| Input factors | Units | Level 1 | Level 2 | Level 3 |
|--------------------------|--------|---------|---------|---------|
| Coded value | - | -1 | 0 | 1 |
| (r) Reinforcement | (wt.%) | 0.23 | 0.45 | 0.67 |
| (v) Cutting speed | m/min | 80 | 95 | 110 |
| (f) Feed rate | mm/rev | 0.04 | 0.1 | 0.16 |
| (a) Depth of cut | mm | 0.04 | 0.1 | 0.16 |

Material removal rate (MRR) and surface roughness (R_a) were the responses. A Mitsubishi-made PCD cutting tool (CCGW09T304-PCD010) was used for machining the nanocomposites in a dry environment. MRR was calculated using Eqn. (4),

$$MRR = \pi \left(\frac{D_i - D_f}{2} \right) \times \left(\frac{D_i + D_f}{2} \right) f N \quad (4)$$

where D_i and D_f are diameters in mm of the specimen before and after the machining, respectively. f is the feed rate (mm/rev), and N is the rotational speed (rpm) [10].

Surface roughness, R_a was measured by using a Talysurf 200 machine with 0.8 mm as cutoff length and 4 mm as evaluation length, according to ISO 4287:1997 standards. R_a is the average roughness from the mean line taken within sampling length [21] and is represented in equation (5) and as a schematic in **Fig. 1**.

$$R_a = \frac{1}{s} \int_0^s |f(x)| \quad (5)$$

The $f(x)$ is the distribution of the height over a length s of the profile [22]. An average value obtained from three trials at each experimental setting is reported as the response values. Multi-objective optimization available in Design-Expert software was used to optimize the surface roughness (R_a) and material removal rate (MRR). This is based on the desirability index. Let X be the set of input process parameters and Y be the fitted response, which is a function of X . Y_H and Y_L are the highest and lowest values of Y . Likewise, there are n responses. Numerical optimization helps to optimize a combination of one

or many goals on the responses. To *minimize* the goal, the individual desirability L is calculated as in Eqn. (6).

$$L = \begin{cases} 1, Y \leq Y_L \\ \left[\frac{Y_H - Y}{Y_H - Y_L} \right], Y_L < Y < Y_H \\ 0, Y \geq Y_H \end{cases} \quad (6)$$

To *maximize* the goal the individual desirability L is calculated as in Eqn. (7).

$$L = \begin{cases} 0, Y \leq Y_L \\ \left[\frac{Y - Y_L}{Y_H - Y_L} \right], Y_L < Y < Y_H \\ 1, Y \geq Y_H \end{cases} \quad (7)$$

A *weight* also has to be assigned to each goal varying from 0.1 to 10. Every goal can be assigned an *importance* varying from + (a value of 1) to +++++ (a value of 5). When there are n responses, to convert this response to a single one, we use the function, F as shown by equation (8) [23]. The shape of desirability function changes with weight as shown in **Fig. 4**.

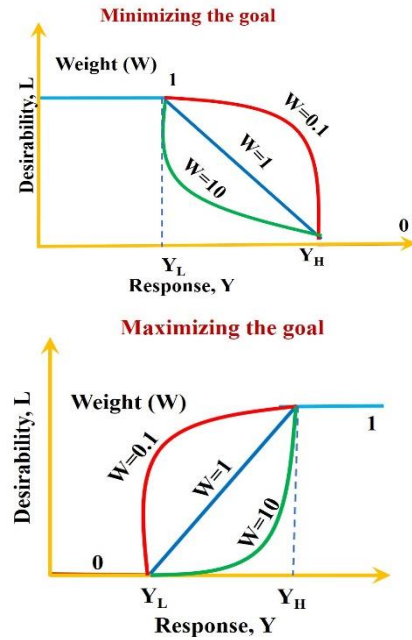


Figure 4. Individual desirability function in minimizing and maximizing the goals

$$F = \left(\prod_{i=1}^n L_i \right)^{\frac{1}{n}} \quad (8)$$

III. RESULTS AND DISCUSSION

The average values of MRR and R_a for each setting of the input factors based on the Box-Behnken design are presented in **Table 4**. These values were analyzed using Design-Expert software. Statistical validation of the models of MRR and R_a is presented

in **Fig. 5**. It is evident that the data points are normally distributed (**Fig. 5 (a)**, **Fig. 5 (b)**) and that the predicted and actual values fall along the straight-line (**Fig. 5 (c)**, **Fig. 5 (d)**), thus ensuring statistical validation of the models of MRR and R_a . For MRR , a model including the individual terms, interaction terms, and square terms of all the input factors was found to be significant by ANOVA analysis. The R^2 and adjusted R^2 of the model were 0.9917 and 0.9821, respectively. The predicted R^2 (of 0.9537) agrees with the adjusted R^2 , since their difference is lesser than 0.2, the model can be used for prediction [24].

Table 4. Input factor settings and the average MRR and R_a values

| Run order | Reinforcement (r) wt. % | Cutting speed (v) (m/min) | Feed rate (f) (mm/r) | Depth of cut (a) (mm) | MRR (mm^3/m) | R_a (μm) |
|-----------|-------------------------|---------------------------|----------------------|-----------------------|--------------------|-------------------|
| 1 | 0.45 | 95 | 0.10 | 0.10 | 899.95 | 0.7095 |
| 2 | 0.45 | 95 | 0.10 | 0.10 | 852.41 | 0.7104 |
| 3 | 0.45 | 95 | 0.10 | 0.10 | 820.7 | 0.6843 |
| 4 | 0.45 | 80 | 0.16 | 0.10 | 1148.83 | 1.1511 |
| 5 | 0.67 | 95 | 0.04 | 0.10 | 353.95 | 0.1912 |
| 6 | 0.67 | 110 | 0.10 | 0.10 | 1006.05 | 0.6977 |
| 7 | 0.67 | 80 | 0.10 | 0.10 | 736.47 | 0.6965 |
| 8 | 0.67 | 95 | 0.16 | 0.10 | 1331.3 | 1.1452 |
| 9 | 0.67 | 95 | 0.10 | 0.16 | 1538.75 | 0.7102 |
| 10 | 0.23 | 95 | 0.10 | 0.04 | 405.97 | 0.7071 |
| 11 | 0.23 | 110 | 0.10 | 0.10 | 1138.35 | 0.7053 |
| 12 | 0.23 | 95 | 0.16 | 0.10 | 1522.64 | 1.1528 |
| 13 | 0.23 | 95 | 0.04 | 0.10 | 395.44 | 0.1851 |
| 14 | 0.23 | 80 | 0.10 | 0.10 | 819.4 | 0.7101 |
| 15 | 0.23 | 95 | 0.10 | 0.16 | 1543.08 | 0.701 |
| 16 | 0.23 | 95 | 0.10 | 0.04 | 431.33 | 0.6962 |
| 17 | 0.45 | 80 | 0.10 | 0.16 | 1215.36 | 0.3067 |
| 18 | 0.45 | 95 | 0.04 | 0.16 | 564.9 | 0.1495 |
| 19 | 0.45 | 110 | 0.10 | 0.16 | 1585.67 | 0.3116 |
| 20 | 0.45 | 95 | 0.16 | 0.16 | 2183.51 | 0.3052 |
| 21 | 0.45 | 110 | 0.16 | 0.10 | 1778.5 | 1.0967 |
| 22 | 0.45 | 80 | 0.04 | 0.10 | 330.57 | 0.1903 |
| 23 | 0.45 | 110 | 0.04 | 0.10 | 427.51 | 0.214 |
| 24 | 0.45 | 95 | 0.16 | 0.04 | 644.33 | 1.0948 |
| 25 | 0.45 | 80 | 0.10 | 0.04 | 262.59 | 0.7232 |
| 26 | 0.45 | 95 | 0.04 | 0.04 | 107.85 | 0.2095 |
| 27 | 0.45 | 110 | 0.10 | 0.04 | 275.54 | 0.7404 |

Adeq Precision is an indicator of signal-to-noise ratio. A value of 39.615 (>4) is an adequate signal which also indicates that the model can be used for prediction. The F -value of model is 102.64 which ensures the significance of the model. There is only a chance of 0.01 % that the F -value was caused by the noise. Equation (9) is the coded regression equation developed for predicting the MRR . The model for R_a including the individual terms of reinforcement wt. % (r), feed rate (f) and depth of cut (a), and interaction term of feed rate and depth of cut, and square term of reinforcement wt. %, r , and depth of cut, a was found to be significant by ANOVA

analysis. The R^2 and adjusted R^2 of the model for R_a were 0.8804 and 0.8445, respectively.

$$\begin{aligned} \text{Material Removal Rate, } MRR = & 857.69 - 39.81r + \\ & 141.53v + \\ & 535.74f + 541.97a \\ & -12.34rv - 37.46rf + 5.26ra + \\ & 133.18vf + \\ & 89.34va + 270.53fa + 67.84r^2 + 5.6v^2 + \\ & 13.66f^2 + 9.85a^2 \end{aligned} \quad (9)$$

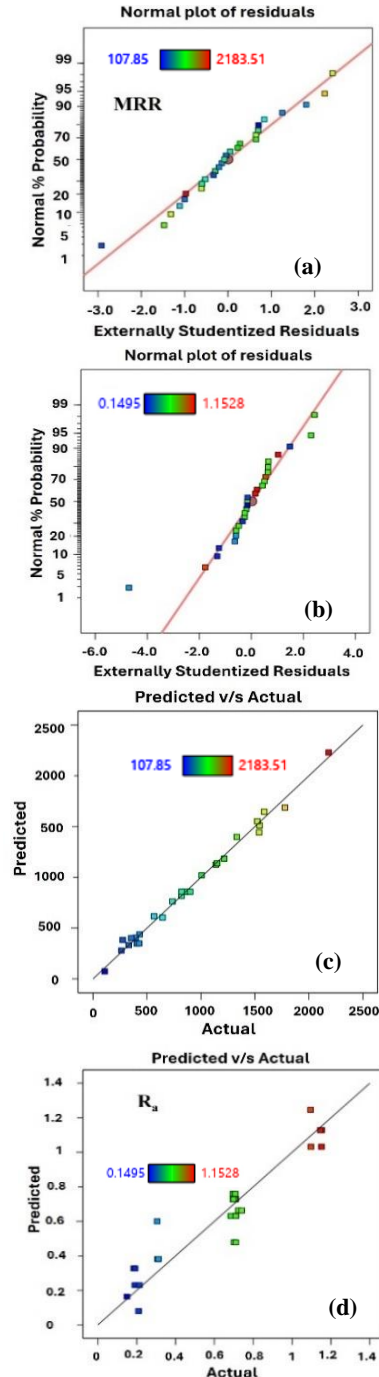


Figure 5. Statistical validation plots (a) Normal Probability of MRR (b) Predicted vs. Actual of MRR (c) Normal Probability of R_a (d) Predicted vs. Actual of R_a

The predicted R^2 (of 0.6641) agrees with the adjusted R^2 , since their difference is lesser than 0.2, the model can be used for prediction [24]. An *Adeq Precision* value of 17.696 (>4) is an adequate signal which also indicates that the model for R_a can be used for prediction. The *F-value* of the model is 24.53 ensuring the significance of the model. There is only a 0.01% chance that the *F-value* was caused by the noise. Equation (10) is the coded regression equation for R_a .

$$\text{Surface Roughness, } R_a = 0.6311 - 0.00022r + 0.4005f - 0.1406a - 0.1824fa + 0.9664r^2 - 0.109a^2 \quad (10)$$

A perturbation plot shows the changes in the values of the response when each factor is moved from the reference value when all the other factors are maintained at their reference value. The steeper the slope is, or the more the curvature is, the more sensitive the response is to the factor. **Fig. 6 (a)** and **Fig. 6 (b)** shows the perturbation plots of MRR and R_a . It is evident that the MRR is more sensitive to feed rate (C) and depth of cut (D) than to the cutting speed (B) and the reinforcement wt.% (A). R_a is more sensitive to feed rate (C) than the depth of cut (D) and reinforcement wt.% (A) since the slopes are higher for the feed rate (C) compared to the slopes of the reinforcement wt.% (A) and depth of cut (D). R_a is not sensitive to changes in cutting speed (B). The regression models obtained for MRR and R_a were validated experimentally. Error % was less than 10 % for MRR and R_a as presented in **Table 5**.

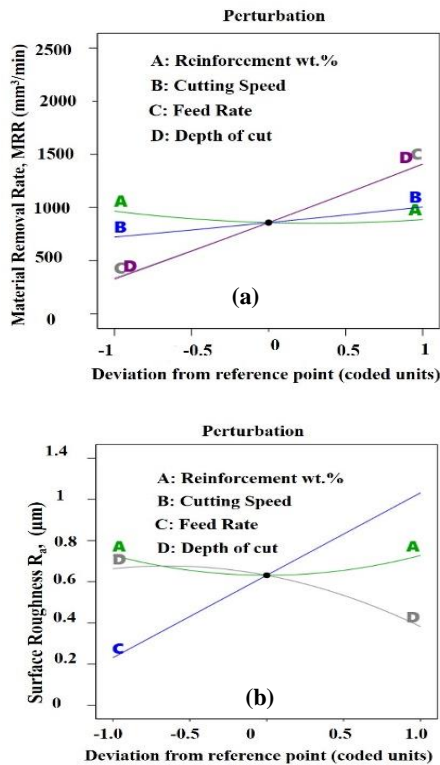


Figure 6. Perturbation plots of (a) MRR and (b) R_a

Table 5. Experimental validation of the models of MRR and R_a

| Reinforcement (r) (wt.%) | Cutting speed (v) (m/min) | Feed rate (f) (mm/re v) | Depth of cut (a) (mm) | MRR Error % | R_a Error % |
|--------------------------|---------------------------|-------------------------|-----------------------|-------------|---------------|
| 0.67 | 80 | 0.16 | 0.08 | 6.75 | 3.57 |
| 0.67 | 100 | 0.08 | 0.16 | 0.81 | 6.02 |

1. Individual effects of reinforcement wt.% (r) on nanocomposite properties, MRR and R_a

Fig. 7(a)-(c) shows the variation in grain size, microhardness, porosity, and density with Si_3N_4 wt.% obtained from the data in **Table 2**.

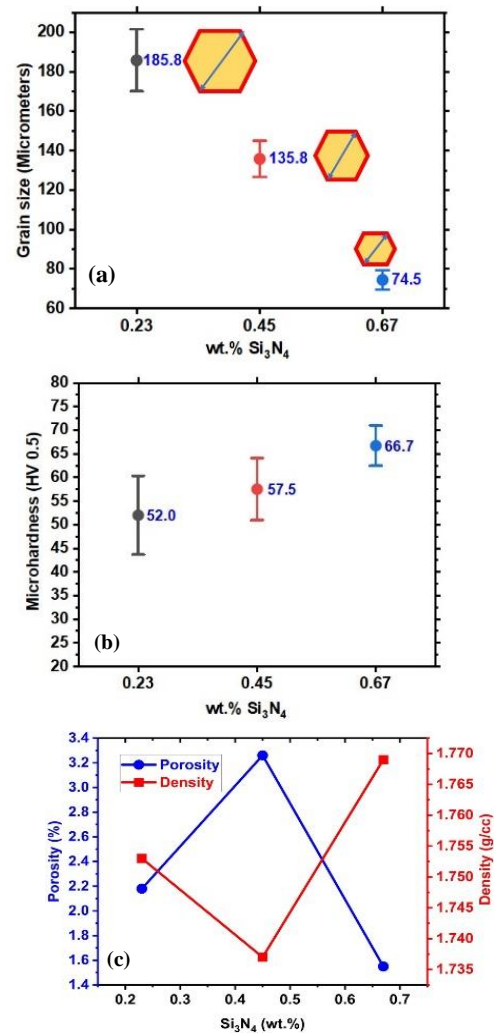


Figure 7. (a) Grain size (b) Microhardness and (c) Porosity and density vs. Si_3N_4 wt.%

The addition of Si_3N_4 reinforcement has influenced the grain size, microhardness, porosity and density. **Fig. 8** shows the main effects of the Si_3N_4 reinforcement wt.% on MRR and R_a and the reasoning for the variation as inset.

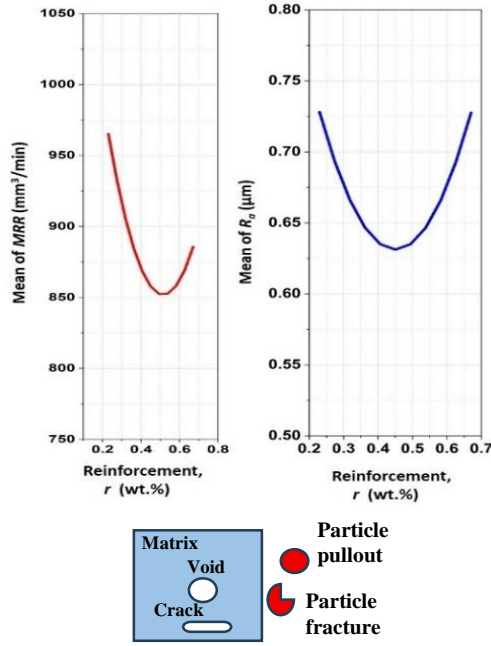


Figure 8. Individual effects of Si_3N_4 wt.% on (a) MRR and (b) R_a and reasoning (inset)

A. Increase of Si_3N_4 (r) from 0.23 to 0.45 wt.%

From **Fig. 7 (a)** and the optical micrographs (**Fig. 3**), it is evident that as the Si_3N_4 reinforcement wt.% (r) is increased from 0.23 to 0.45 wt.%, the grain size decreased. This is attributed to the Si_3N_4 particles acting as heterogeneous nucleating sites within the Mg grains and restricting the growth of grains as observed by Viswanath et al. [25]. This has also increased vickers microhardness (**Fig. 7 (b)**) due to the increased resistance to deformation caused by the restriction of the dislocation movement by the Si_3N_4 nanoparticles [26] and agrees with the findings of Mistry et al. [26]. The porosity has also increased (**Fig. 7 (c)**) due to the increased number of particles increasing the viscosity of the melt, which prevents the air/gas trapped from escaping the melt and results in increased porosity as observed by Aravindan et al. [27] which has decreased the actual density (**Fig. 7 (c)**). The increase in porosity softens the material. Therefore, as r is increased from 0.23 to 0.45 wt.%, there are two possible effects:

- (i) Hardening effect on material characterized by increase in microhardness caused by reduction in grain size.
- (ii) Softening effect of material due to increase in porosity.

Among these two effects, any one can predominate over the other, which would impact the MRR and R_a . From **Fig. 8 (a)** and **Fig. 8 (b)** respectively, it is evident that as r is increased from 0.23 to 0.45 wt.%, MRR decreased and R_a also decreased. This is because the hardening effect has predominantly influenced the MRR over the softening effect, due to

which material removal became difficult which reduced MRR . Since less material was removed by the tool, the nanoparticles remained intact in the matrix. This prevented the formation of voids, fracture of particles, dragging of particles over the surface etc. thereby reducing the surface roughness, R_a [21], [28] (**Fig. 8 (inset)**).

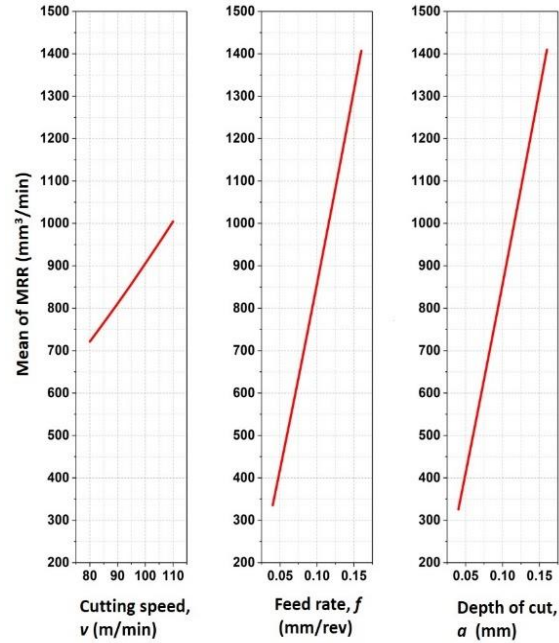


Figure 9. Individual effects of cutting speed, v , feed rate, f , and depth of cut, a , on MRR

B. Increase of Si_3N_4 (r) from 0.45 to 0.67 wt.%

From **Fig. 7 (a)**, it is evident that as the Si_3N_4 reinforcement wt.% (r) is increased from 0.45 to 0.67 wt.%, the grain size decreased further and increased the microhardness (**Fig. 7 (b)**) due to the increased heterogeneous nucleation and hence increased deformation resistance. **Fig. 7 (c)** shows that as the Si_3N_4 reinforcement wt.% (r) is increased from 0.45 to 0.67 wt.%, the porosity has decreased due to the effects of increased wetting between the nanoparticles and the matrix which predominated the effects of viscosity, and hence decreased the porosity, as observed by Tosun et al. [29], thereby increasing the actual density (**Table 1**). However, as r is increased from 0.45 to 0.67 wt.%, MRR and R_a increase (**Fig. 8 (a)** and **Fig. 8 (b)**) which means more material has been removed and surface quality has decreased. This could be explained as below:

In the range of 0.45 to 0.67 reinforcement wt.%, the below effects are operating

- (i) Hardening effect on material characterized by increase in microhardness caused by reduction in grain size.
- (ii) Hardening effect of material due to decrease in porosity.

- (iii) Softening effect caused by increased dislodging of reinforcement particles from the matrix.

Any of these three effects could predominantly influence MRR and R_a over the other two. With the increase in reinforcement wt.% (r) from 0.45 to 0.67 wt.% i.e. the no. of reinforcement particles have increased, which also increases the probability of particle dislodging. This results in increased dislodging of particles, which could soften the material and increase the voids, particle pullout [28], particle fracture, dragging of particles over the surface [21] [28] as shown in **Fig. 8** (inset) which softened the material and increased the ease of material removal (hence MRR), decreased surface quality, and hence increase in the surface roughness, R_a . Similar phenomenon was observed by Sikder et al. [28] and Anandan et al. [21].

Fig. 9 shows the individual effects of the cutting speed, v , feed rate, f , and depth of cut, a , on MRR . It is evident that as v , f , and a are increased, MRR increases. This is due to the enhanced amount of material removed in less time in the directions of v , f , and a . **Fig. 10** shows the main (individual) effects of the cutting speed, v , feed rate, f , and depth of cut, a , on R_a . As f is increased from 0.04 to 0.16 mm/rev, R_a increases.

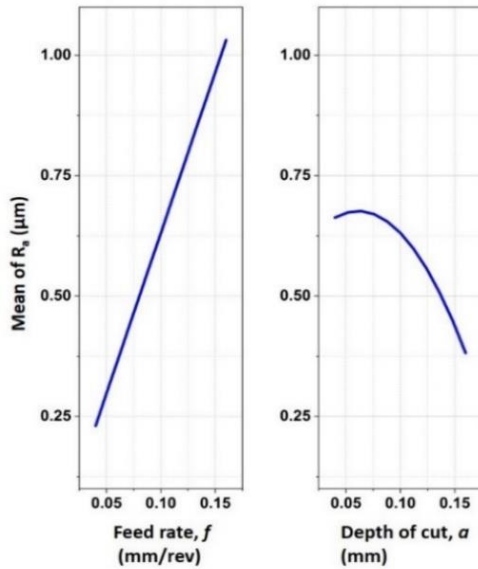


Figure 10. Individual effects of cutting speed, v , feed rate, f , and depth of cut, a , on R_a

This is due to one or more of these reasons: (i) feed marks, (ii) surface defects like voids (because of particle pullout), (iii) cracking of the metal matrix (due to low ductility), and (iv) hard reinforcement [21]. As the depth of cut (a) increases from 0.04 mm, R_a first slightly increases due to the effects of heavy pressure and abrasion around the cutting edge and extrusion below the cutting edge which caused the roughness of the surface to increase, and increases the R_a . After this initial rise, R_a decreases steeply

with depth of cut, a because the area of contact between the work and the cutting edge increases the components of the forces as observed by Shoba et al. [30]. This could have caused more cutting resistance, causing the cutting tool to make fewer impressions/undulations over the work surface resulting in lesser R_a .

2. Interactive effects of input factors on MRR and R_a

Fig. 11 and **Fig. 12** show the interactive effects of input factors on MRR . A , B , C , and D represent the corners of the response surfaces. The reasoning for variations in MRR and R_a , with changes in the input factors discussed in the individual effects, are applicable here too. The reinforcement wt.% is abbreviated as r , cutting speed as v , feed rate as f , and depth of cut as a .

Fig. 11 (a) shows the 3D plot of interactive effects of r and v on the MRR when f and a are held at their mid-levels. At low v (along AB) and high v (along DC), MRR decreases, reaches a minimum value, and then increases with r non-linearly. At low r (along AD) and high r (along BC), MRR increases with v . Higher MRR is obtained at lower r and higher v . **Fig. 11 (b)** shows the 3D plot of interactive effects of r and f , on the MRR when v , and a are held at their mid-levels. At a low f (along AB), MRR decreases and reaches a minimum value, and then it increases curvilinearly with r . At high f (along DC), MRR decreases curvilinearly with r . At low r (along AD) and high r (along BC), MRR increases with f . Higher MRR is obtained towards lower r and higher f . **Fig. 11 (c)** shows the 3D plot of interactive effects of r , and a , on the MRR when f , and v , are held at their mid-levels. At low a (along AB) and high a (along DC), MRR decreases first and then increases curvilinearly with r . At low r (along AD) and high r (along BC), the MRR increases with a linearly. Higher MRR is obtained at low r and high a .

Fig. 12 (a) shows the 3D plot of interactive effects of f and v on the MRR when r , and a , are held at their mid-levels. At low f (along AB), MRR shows a very slight increase when v is increased. At high f (along DC), MRR increases with v , almost linearly. At low v (along AD), MRR increases with f . At high v (along BC), the MRR increases with f . Higher MRR is obtained at higher v and higher f . **Fig. 12 (b)** shows the 3D plot of interactive effects of f , and a , on the MRR when r , and v , are held at their mid-levels. At low a (along AB), MRR increases (almost linearly) with f . At high a (along DC), the MRR increases more steeply with f . At a low f (along AD), the MRR increases (almost linearly) with a . At high f (along BC), the MRR increases more steeply with a . Higher MRR is obtained towards higher f and higher a . **Fig. 12 (c)** shows the 3D plot of interactive effects of a , and v , on the MRR when r and f , are held at their mid-

levels. At low a (along AB), MRR increases slightly almost linearly with v .

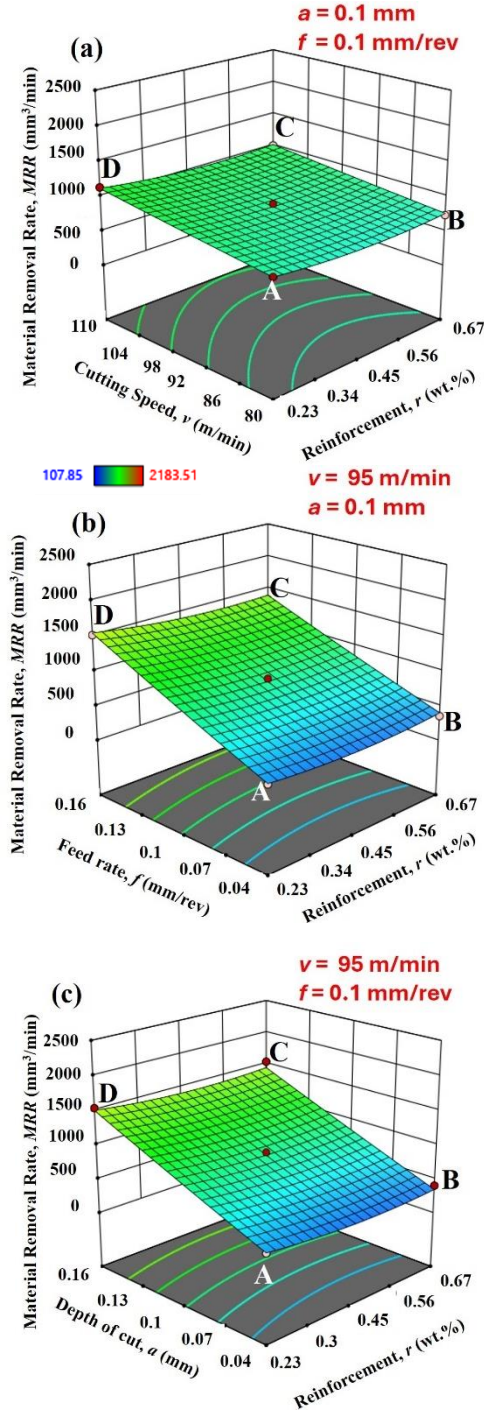


Figure 11. Interactive effects of (a) v and r (b) f and r (c) a and r on MRR

At high a (along DC), the MRR increases almost linearly with v . At low v (along AD), MRR increases almost linearly with a . At high v (along BC), MRR increases almost linearly with a . Higher MRR is achieved with higher a and higher v . **Fig. 13** shows the interactive effects of f and a on R_a . The model for R_a indicates that only the interaction between the feed rate (f) and depth of cut (a) is significant. R_a

increases with f for lower a (along AB) and higher a (along DC).

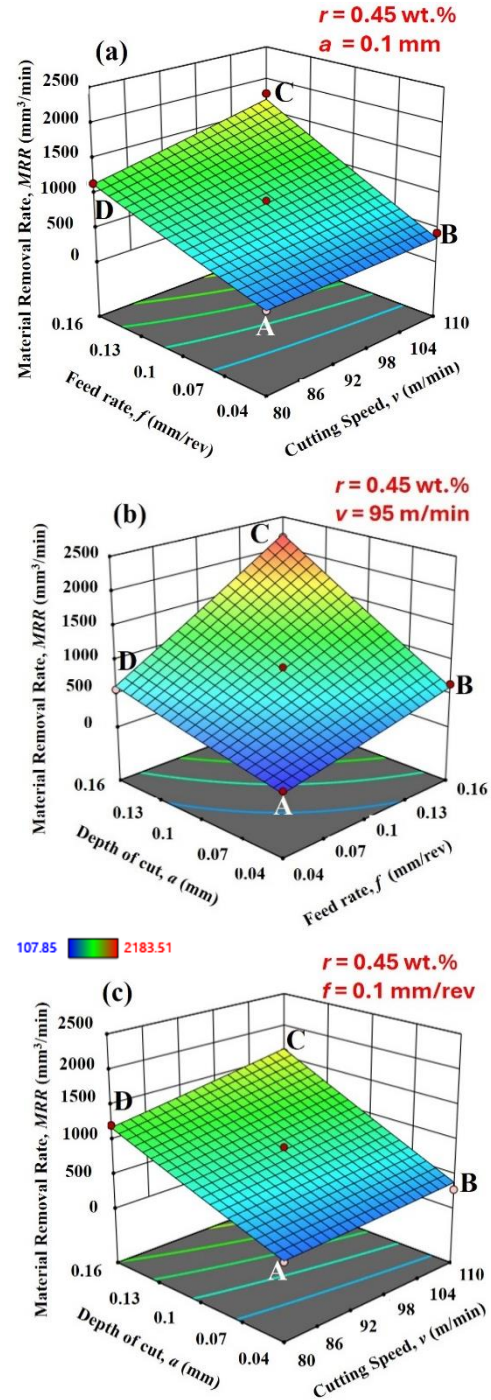


Figure 12. Interactive effects of (a) v and f (b) f and a (c) a and v on MRR

At low f , (along AD), as a increases, R_a first slightly increases and then decreases. At higher f (along BC), R_a decreases non-linearly with a . Lower R_a is obtained at lower f and also lower a .

Multi-objective optimization using Design-Expert software was done with the input factors (*in range*), *MRR* (Weight: 4 Importance: ++) and *R_a* (Weight: 7 Importance: +++) to maximize *MRR* and minimize *R_a*. Fig. 14 shows the optimization ramp. Si₃N₄ nanoparticle addition of 0.44 wt.%, cutting speed of 110 m/min, feed rate of 0.09 mm/rev, and depth of cut of 0.16 mm were suitable in the sustainable, economical machining of Mg-4Zn/Si₃N₄ nanocomposites with good surface quality.

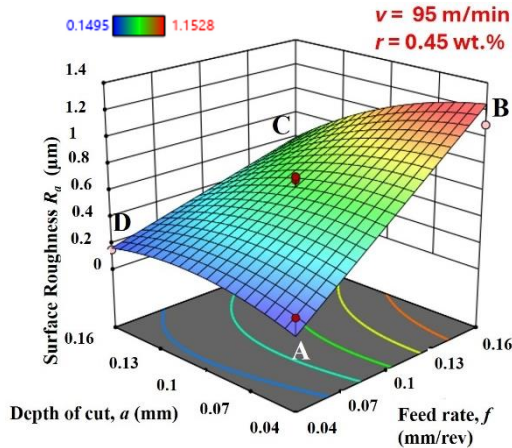


Figure 13. Interactive effects of *f* and *a* on *R_a*

The optimal *MRR* is 1446.29 mm³/min and optimal *R_a* is 0.3351 μm. Confirmation experiments of *MRR* and *R_a* at the optimal parameter setting yielded an error of 9.64 % and 7.01% respectively.

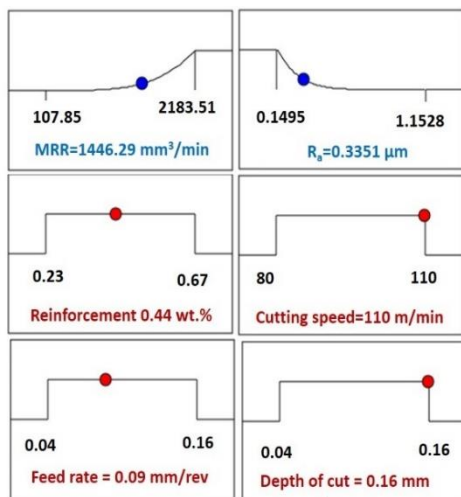


Figure 14. Optimization ramps showing the optimized *MRR*, *R_a*, and the input process parameters

IV. CONCLUSIONS

The improvement in microhardness and variation in porosity levels caused by the Si₃N₄ nanoparticle additions, and also the dry turning parameters influenced the material removal rate (*MRR*) and

surface roughness (*R_a*). Regression models for prediction of *MRR* and *R_a* were obtained.

The models were studied using ANOVA and validated statistically and experimentally (with error less than 10%). This showed that the Si₃N₄ reinforcement wt.% and machining parameters and their interactions significantly affected the *MRR*. The model for *MRR* of linear, square, and interaction terms of the reinforcement wt.%, cutting speed, feed rate, and depth of cut. *R_a* was influenced by the feed rate and depth of cut and their interaction also by the Si₃N₄ reinforcement wt.% (square term) as confirmed by the regression model. Higher *MRR* was obtained at a lower level of Si₃N₄ additions and higher levels of *v*, *f*, and *a*. Lower *R_a* is obtained at lower feed rates and lower depths of cut (from interactive plots).

Multi-objective optimization of *MRR* and *R_a* revealed that for obtaining a higher material removal rate and good surface quality, medium reinforcement (0.44 wt.%), higher cutting speed (110 m/min), medium feed rate (0.09 mm/rev), and higher depth of cut (0.16) are preferred to obtain a material removal rate of 1446.29 mm³/min and surface roughness *R_a* of 0.3351 μm.

ACKNOWLEDGEMENT

The authors duly acknowledge APJ Abdul Kalam Technological University (APJAKTU), Thiruvananthapuram, Kerala, Center for Engineering Research and Development (CERD), (APJAKTU), Thiruvananthapuram, College of Engineering Trivandrum, Nanoshel UK Limited, Intelligent Materials Pvt Ltd, Punjab (for nanomaterials), SwamEquip, Chennai and Mr. Venkat Raghavan of SwamEquip (for stir casting), Central Instrumentation Facility (CIF), Indian Institute of Technology (IIT) Palakkad, and its staff, Mr. Mejo A. J, Central Laboratory for Instrumentation and Facilitation (CLIF), University of Kerala, Thiruvananthapuram, Sophisticated Test and Instrumentation Center (STIC India, CUSAT, Cochin) and its scientist Dr. Shibu M Eappen, Agro Met Lab, Coimbatore and its technical manager, Mr. R. Arunkumar and Chennai Metco, Chennai for materials studies, Zenith Industrial Solutions, Chennai and its staff Mr. Sivakumar K, Mitsubishi Materials Corporation, ISRO Inertial Systems Unit (IISU), Thiruvananthapuram, Mr. Joji J Chaman and Precision Instrumentation Laboratory (PIL), IISU (for machining and materials studies), Stat-Ease, Inc, Systech Technocraft Services Pvt. Ltd., Mumbai for Design-Expert software, OriginLab Corporation, Konark Solutions Bangalore Pvt Ltd. for OriginLab and ImageJ for supporting this research.

AUTHOR CONTRIBUTIONS

N Anand: Conceptualization, Experiments, Theoretical analysis, Writing, Review and Editing.

K Jayprakash Reddy: Experiments, Theoretical Analysis, Review and editing.

D Bijulal: Supervision, Theoretical Analysis, Review and editing.

K Vijayan: Supervision, Theoretical Analysis, Review and editing.

P Prasanth: Experiments, Theoretical Analysis, Review and editing.

DISCLOSURE STATEMENT

The authors declare that they have no known competing financial interests or personal relationships that could have appeared to influence the work reported in this paper.

ORCID

N Anand <https://orcid.org/0009-0004-3356-9946>

K Jayaprakash Reddy <https://orcid.org/0000-0001-6540-141X>

D Bijulal <https://orcid.org/0000-0003-2712-3097>

K Vijayan <https://orcid.org/0009-0001-2037-2720>

P Prasanth <https://orcid.org/0009-0004-0940-595X>

REFERENCES

- [1] P. Nyamekye, R. Lakshmanan, V. Tepponen, and S. Westman, "Sustainability aspects of additive manufacturing: Leveraging resource efficiency via product design optimization and laser powder bed fusion," *Heliyon* 10 (1) (2024) e23152. <https://doi.org/10.1016/j.heliyon.2023.e23152>
- [2] G. Parande, V. Manakari, S. D. Sharma Kopparthy, and M. Gupta, "A study on the effect of low-cost eggshell reinforcement on the immersion, damping and mechanical properties of magnesium–zinc alloy," *Compos B Eng* 182 (2020) 107650. <https://doi.org/10.1016/j.compositesb.2019.107650>
- [3] J. Song, J. She, D. Chen, and F. Pan, "Latest research advances on magnesium and magnesium alloys worldwide," *Journal of Magnesium and Alloys* 8 (1) (2020) pp. 1-41. <https://doi.org/10.1016/j.jma.2020.02.003>
- [4] R. Radha and D. Sreekanth, "Insight of magnesium alloys and composites for orthopedic implant applications – a review," *Journal of Magnesium and Alloys* 5 (3) (2017) pp. 286–312. <https://doi.org/10.1016/j.jma.2017.08.003>
- [5] S. García-Rodríguez, B. Torres, A. Maroto, A. J. López, E. Otero, and J. Rams, "Dry sliding wear behavior of globular AZ91 magnesium alloy and AZ91/SiCp composites," *Wear* 390–391 (2017) pp. 1-10. <https://doi.org/10.1016/j.wear.2017.06.010>
- [6] N. M. Chelliah, H. Singh, and M. K. Surappa, "Correlation between microstructure and wear behavior of AZX915 Mg-alloy reinforced with 12 wt% TiC particles by stir-casting process," *Journal of Magnesium and Alloys* 4 (4) (2016) pp. 306-313. <https://doi.org/10.1016/j.jma.2016.09.002>
- [7] J. Hashim, L. Looney, and M. S. J. Hashmi, "Metal matrix composites: production by the stir casting method," *J Mater Process Technol* 92–93 (1999) pp. 1–7. [https://doi.org/10.1016/S0924-136\(99\)00118-1](https://doi.org/10.1016/S0924-136(99)00118-1)
- [8] Y. Qiao, N. Fan, P. Guo, Y. Bai, and S. Wang, "Surface integrity analysis in turning A03190/304 composites with network reinforcement," *Engineering Science and Technology, an International Journal* 19 (4) (2016) pp. 1960-1970. <https://doi.org/10.1016/j.jestch.2016.07.017>
- [9] S. A. Bagaber and A. R. Yusoff, "Energy and cost integration for multi-objective optimisation in a sustainable turning process," *Measurement (Lond)* 136 (2019) pp. 795-810. <https://doi.org/10.1016/j.measurement.2018.12.096>
- [10] G. C. Manjunath Patel, D. Lokare, G. R. Chate, M. B. Parappagoudar, R. Nikhil, and K. Gupta, "Analysis and optimization of surface quality while machining high strength aluminium alloy," *Measurement (Lond)* 152 (2020) 107337. <https://doi.org/10.1016/j.measurement.2019.107337>
- [11] A. T. Abbas, D. Y. Pimenov, I. N. Erdakov, M. A. Taha, M. S. Soliman, and M. M. El Rayes, "ANN Surface Roughness Optimization of AZ61 Magnesium Alloy Finish Turning: Minimum Machining Times at Prime Machining Costs," *Materials* 11 (5) (2018) 808. <https://doi.org/10.3390/ma11050808>
- [12] D. Kumar and R. K. Porwal, "Parametric Optimization of Thermoelectric Machining of Stir-Cast Hybrid Magnesium Metal Matrix Composite with Alumina and Silicon

- Carbide as Reinforcement,” *Journal of The Institution of Engineers (India): Series D* 105 (3) (2024) pp. 1927–1943.
<https://doi.org/10.1007/s40033-023-00628-x>
- [13] S. Sudhagar, P. M. Gopal, M. Maniyarasan, S. Suresh, and V. Kavimani, “Multi-objective optimization of machining parameters for Si₃N₄–BN reinforced magnesium composite in wire electrical discharge machining,” *International Journal on Interactive Design and Manufacturing (IJIDeM)* 18 (7) (2024) pp. 4787–4802.
<https://doi.org/10.1007/s12008-024-01777-3>
- [14] S. Zhang *et al.*, “Research on an Mg–Zn alloy as a degradable biomaterial,” *Acta Biomater* 6 (2) (2010) pp. 626–640.
<https://doi.org/10.1016/j.actbio.2009.06.028>
- [15] J. Wang, Y. Ma, S. Guo, W. Jiang, and Q. Liu, “Effect of Sr on the microstructure and biodegradable behavior of Mg–Zn–Ca–Mn alloys for implant application,” *Mater Des* 153 (2018) pp. 308–316.
<https://doi.org/10.1016/J.MATDES.2018.04.062>
- [16] B. P. Zhang, Y. Wang, and L. Geng, “Research on Mg–Zn–Ca Alloy as Degradable Biomaterial,” in *Biomaterials*, R. Pignatello, Ed., Rijeka: IntechOpen, 2011, ch. 9.
<https://doi.org/10.5772/23929>
- [17] F. L. Riley, “Silicon Nitride and Related Materials,” *Journal of the American Ceramic Society* 83 (2) (2000) pp. 245–265.
<https://doi.org/10.1111/j.1151-2916.2000.tb01182.x>
- [18] M. Paramsothy, J. Chan, R. Kwok, and M. Gupta, “Enhanced mechanical response of hybrid alloy \emph{AZ31/AZ91} based on the addition of Si₃N₄ nanoparticles,” *Materials Science and Engineering: A* 528 (21) (2011) pp. 6545–6551.
<https://doi.org/10.1016/j.msea.2011.05.003>
- [19] L. Fu *et al.*, “Biodegradable Si₃N₄ bioceramic sintered with Sr, Mg and Si for spinal fusion: Surface characterization and biological evaluation,” *Appl Mater Today* 12 (2018) pp. 260–275.
<https://doi.org/10.1016/J.APMT.2018.06.002>
- [20] K. H. Park, A. Beal, D. D. W. Kim, P. Kwon, and J. Lantrip, “Tool wear in drilling of composite/titanium stacks using carbide and polycrystalline diamond tools,” *Wear* 271 (11–12) (2011) pp. 2826–2835.
<https://doi.org/10.1016/J.WEAR.2011.05.038>
- [21] N. Anandan and M. Ramulu, “Study of machining induced surface defects and its effect on fatigue performance of AZ91/15%SiCp metal matrix composite,” *Journal of Magnesium and Alloys* 8 (2) (2020) pp. 387–395.
<https://doi.org/10.1016/j.jma.2020.01.001>
- [22] B. Ozcelik, H. Oktem, and H. Kurtaran, “Optimum surface roughness in end milling Inconel 718 by coupling neural network model and genetic algorithm,” *The International Journal of Advanced Manufacturing Technology* 27 (3) (2005) pp. 234–241.
<https://doi.org/10.1007/s00170-004-2175-7>
- [23] Statease, “DesignExpert optimization.” Accessed: May 19, 2025. [Online]. Available:
<https://www.statease.com/docs/v23.1/contents/optimization/desirability-details/>
- [24] R. Mehra, H. Singh, and S. K. Chaubey, “Evaluating Surface Roughness of Ductile Cast Iron Machined by EDM Using Solid and Hollow Cylindrical Copper Electrodes,” *Periodica Polytechnica Mechanical Engineering* 69 (1) (2025) pp. 46–54.
<https://doi.org/10.3311/PPme.38763>
- [25] A. Viswanath, H. Dieringa, K. K. Ajith Kumar, U. T. S. Pillai, and B. C. Pai, “Investigation on mechanical properties and creep behavior of stir cast AZ91–SiCp composites,” *Journal of Magnesium and Alloys* 3 (1) (2015) pp. 16–22.
<https://doi.org/10.1016/j.jma.2015.01.001>
- [26] J. M. Mistry and P. P. Gohil, “Experimental investigations on wear and friction behaviour of Si₃N₄p reinforced heat-treated aluminium matrix composites produced using electromagnetic stir casting process,” *Compos B Eng* 161 (2019) pp. 190–204.
<https://doi.org/10.1016/J.COMPOSITESB.2018.10.074>
- [27] S. Aravindan, P. V. Rao, and K. Ponappa, “Evaluation of physical and mechanical properties of AZ91D/SiC composites by two step stir casting process,” *Journal of Magnesium and Alloys* 3 (1) (2015) pp. 52–62.
<https://doi.org/10.1016/j.jma.2014.12.008>
- [28] S. Sikder and H. A. Kishawy, “Analytical model for force prediction when machining metal matrix composite,” *Int J Mech Sci* 59 (1) (2012) pp. 95–103.
<https://doi.org/10.1016/j.ijmecsci.2012.03.010>

- [29] G. Tosun and M. Kurt, “The porosity, microstructure, and hardness of Al-Mg composites reinforced with micro particle SiC/Al₂O₃ produced using powder metallurgy,” *Compos B Eng* 174 (2019) 106965.
<https://doi.org/10.1016/j.compositesb.2019.106965>
- [30] C. Shoba, N. Ramanaiah, and D. Nageswara Rao, “Effect of reinforcement on the cutting forces while machining metal matrix composites—An experimental approach,” *Engineering Science and Technology, an International Journal* 18 (4) (2015) pp. 658–663.
<https://doi.org/10.1016/J.JESTCH.2015.03.013>



This article is an open access article distributed under the terms and conditions of the Creative Commons Attribution NonCommercial (CC BY-NC 4.0) license.